COBEM 2021 26th International Congress of Mechanical Engineering
November 22-26, 2021, Virtual Congress, Brazil

COBEM-2021-0181
NUMERICAL SIMULATION OF IMPINGING SHOCK WAVE / BOUNDARY LAYER INTERACTION USING MACCORMACK TECHNIQUE

Ana Maria Pereira Lara
Instituto Tecnológico de Aeronáutica, São José dos Campos, São Paulo, 12228-900, Brasil
Instituto de Estudos Avançados, São José dos Campos, São Paulo, 12228-001, Brasil
anamariapereiralara@gmail.com

Tiago Cavalcanti Rolim
Instituto de Estudos Avançados, São José dos Campos, São Paulo, 12228-900, Brasil
tiagotcr@fab.mil.br

Abstract. *The objective of this work was to numerically study the oblique shock wave/boundary layer interaction and boundary layer separation caused by impinging shock waves. It was used the explicit solution of the finite differences scheme of the complete two-dimensional laminar Navier-Stokes equations, without body forces and volumetric heating. Also, the following considerations were made for solving the system: calorically perfect gas, Sutherland's law for viscosity, and a constant Prandtl number. The adopted configuration was a supersonic flow with an impinging shock wave on a flat plate. During the tests, it was considered cold and adiabatic wall conditions with the selected freestream Mach numbers of 5, 6, 7 and 8. The impinging shock wave angle varied from 10 to 20 deg. The computer code was developed in MATLAB language using MacCormack's marching technique. The adopted computational domain was a rectangular structured configuration. From the results, it was noticed that the shock wave could be identified by the jump on the pressure profile, and the highest temperature values were near the flat plate surface. Also, higher pressure and temperature values were encountered for the adiabatic wall case. At the considered Mach number range, at particular angles, the shock wave increase in pressure was high enough to produce boundary layer separation zones, characterized by the presence of a pressure plateau and velocity inversion. Near those zones, it was also observed the flow expansion and further reattachment of the boundary layer.*

Keywords: *Hypersonic flow, shock wave, boundary layer, MacCormack's technique.*

1. INTRODUCTION

When a vehicle is at supersonic or hypersonic speeds, there is the formation of shock waves and so, their interaction with the boundary layer. One of the common ways this happens is through an externally generated shock wave that impinges on vehicle's surface. These regions of interaction are characterized by large pressure and heat flux values, which makes this phenomenon of paramount importance for the structural and thermal protection design of any aerospace vehicle.

Boundary layer analysis must be considered during design development due its detrimental impact during flight. If separation occurs, it can cause loss of control, peak thermomechanical loads on the surface and instabilities that can interfere with the vehicle's structure. In internal flows, as in the scramjet engine, separation can increase losses and pressure distortion, inversion and sudden changes in flow properties that could cause inlet unstart (GAITONDE, 2013). In fact, considering these engines, the inlet flow quality is very critical to their overall efficiency. The boundary layer can decrease the inlet mass flow rate which reduces the amount of oxygen that would be used for combustion, leading to, for instance, loss of thrust, specific impulse and even control.

The interaction of a boundary layer with an oblique shock wave produces several flow features as noticed by Babinsky and Harvey (2011). Figure 1 shows a sketch of a shock wave boundary layer interaction with no separation. Regarding this figure, there is an incidence of a shock wave (C_1) that continues to curve (due the decrease in Mach number as it approaches the wall) until its disappearance in the sonic line. The shock wave causes an increase in pressure upstream of the shock, which is transmitted along the flow through the subsonic part of the boundary layer. The dilation of the subsonic region acts as a ramp, forming compression waves (η) that come together to form the reflected shock (C_2). In this case, the interaction resists the adverse pressure gradient and flow separation is not observed.

In Figure 2, the structure of a flow which the incidence of a shock wave causes the separation of the boundary layer is represented. The adverse pressure gradient causes flow reversal and boundary layer separation. The separation bubble

delimits the region with flow recirculation, between separation (S) and reattachment (R). The shock wave (C_4) impinges the separated flow and is reflected as expansion waves. Moreover, compression waves are formed downstream the reattachment point.

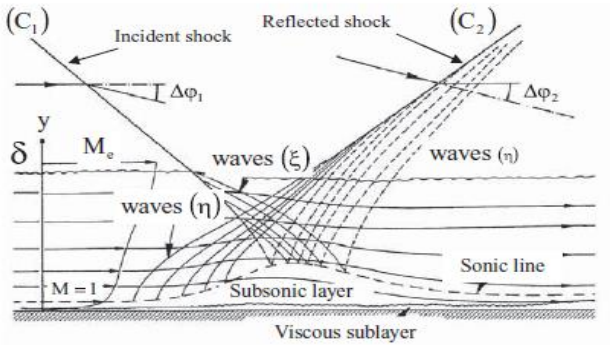

Figure 1 Scheme of shock wave/boundary layer interaction, shock wave impinging on the surface with layer without separation (BABINSKY; HARVEY, 2011).

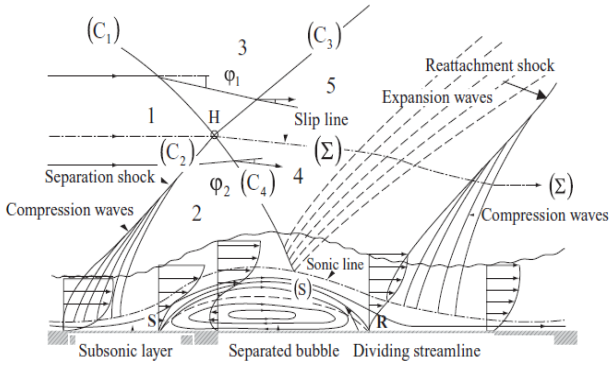

Figure 2. Scheme of shock wave/boundary layer interaction, shock wave impinging on the surface with layer separation (BABINSKY; HARVEY, 2011).

The main objective of this work was to numerically study the shock wave / boundary layer interaction. To achieve this, the following steps were taken: i) it was adopted an explicit finite difference solution of the complete two-dimensional Navier-Stokes equations using the MacCormack's time marching technique considering a laminar boundary layer, ii) the flow caused by impinging shock waves on different Mach numbers and deflection angles was simulated by imposing the correct boundary conditions using the oblique shock wave relations, iii) the profiles, contours plots and numerical schlieren images of the main flow properties were investigated.

2. METHODOLOGY

2.1 NAVIER-STOKES EQUATIONS

This work used the explicit finite difference solution of the two-dimensional Navier-Stokes equations: continuity, momentum in x, momentum in y and energy, with no body forces and no volumetric heating (ANDERSON JR, 1995):

$$\frac{\partial \rho}{\partial t} + \frac{\partial}{\partial x}(\rho u) + \frac{\partial}{\partial y}(\rho v) = 0 \tag{1}$$

$$\frac{\partial}{\partial t}(\rho u) + \frac{\partial}{\partial x}(\rho u^2 + p - \tau_{xx}) + \frac{\partial}{\partial y}(\rho uv - \tau_{yx}) = 0 \tag{2}$$

$$\frac{\partial}{\partial t}(\rho v) + \frac{\partial}{\partial x}(\rho uv - \tau_{xy}) + \frac{\partial}{\partial y}(\rho v^2 + p - \tau_{yy}) = 0 \tag{3}$$

$$\frac{\partial}{\partial t}(E_t) + \frac{\partial}{\partial x}\left[(E_t + p)u + q_x - u\tau_{xx} - v\tau_{xy}\right] + \frac{\partial}{\partial y}\left[(E_t + p)v + q_y - u\tau_{yx} - v\tau_{yy}\right] = 0 \tag{4}$$

So, the equations are function the pressure (p), velocitiy components (u, v), density (ρ), shear stresses $(\tau_{xy}, \tau_{yx}, \tau_{xx})$, total energy per unit volume (E_t) and heat fluxes (q_x, q_y).

E_t is phisically composed by two parcels, one accounts for the internal energy and the other one for the kinetic energy:

$$E_t = \rho\left(e + \frac{V^2}{2}\right) \tag{5}$$

where, e is the internal energy per unit mass and $V^2 = u^2 + v^2$.

The components of the heat flux vector q_x and q_y (following the Fourier's law) are calculated as functions of the temperature (T) and the thermal conductivity (k):

$$q_x = -k\frac{\partial T}{\partial x} \tag{6}$$

$$q_y = -k\frac{\partial T}{\partial y} \tag{7}$$

Considering a laminar flow, shear stresses (STOKES, 1880) are represented in terms of:

$$\tau_{xy} = \tau_{yx} = \mu\left(\frac{\partial u}{\partial y} + \frac{\partial v}{\partial x}\right) \tag{8}$$

$$\tau_{xx} = \lambda(\nabla . V) + 2\mu\frac{\partial u}{\partial x} \tag{9}$$

$$\tau_{yy} = \lambda(\nabla . V) + 2\mu\frac{\partial v}{\partial y} \tag{10}$$

The terms μ and λ are the dynamic viscosity and volumetric viscosity coefficient, respectivelly.

The volumetric viscosity coefficient was calculated using:

$$\lambda = -\frac{2}{3}\mu \tag{11}$$

The Navier-Stokes equations are four equations with nine unknowns. Therefore, the following considerations were done to solve the system:

i) Ideal gas, so the equation of state can be written as:

$$p = \rho RT \tag{12}$$

where R is the gas constant.

ii) Calorically perfect gas,

$$e = c_v T \tag{13}$$

where c_v is the specific heat at constant volume.

iii) Sutherland's law to calculcate dynamic viscosity,

$$\mu = \mu_r\left(\frac{T}{T_r}\right)^{3/2}\frac{T_r + S}{T + S} \tag{14}$$

where S is the Sutherland's constant and subscript r refers to the properties at sea level.

iv) Assuming that Prandtl number was constant, the thermal conductivity could be calculated by:

$$Pr = \frac{\mu c_p}{k} = 0.71 \tag{15}$$

where c_p is the specific heat at constant pressure.

Thus, there are nine unknowns with nine equations which can be written in a vector notation by:

$$\frac{\partial U}{\partial t} + \frac{\partial E}{\partial x} + \frac{\partial F}{\partial y} = 0 \tag{16}$$

Where the column vectors U, E e F were obtained by:

$$U = \begin{Bmatrix} \rho \\ \rho u \\ \rho v \\ E_t \end{Bmatrix} \tag{17}$$

$$E = \begin{Bmatrix} \rho u \\ \rho u^2 + p - \tau_{xx} \\ \rho uv - \tau_{xy} \\ (E_t + p)u - u\tau_{xx} - v\tau_{xy} + q_x \end{Bmatrix} \tag{18}$$

and,

$$F = \begin{Bmatrix} \rho v \\ \rho uv - \tau_{xy} \\ \rho v^2 + p - \tau_{yy} \\ (E_t + p)v - u\tau_{xy} - v\tau_{yy} + q_y \end{Bmatrix} \tag{19}$$

2.2 MACCORMACK'S TECHNIQUE

MacCormack's technique consists of a time march to the steady state solution, finding the flow properties at each spatial location (i, j) of the discretized domain. According to Anderson (1995), the MacCormack's technique can be applied using the steps, firstly, prediction at time $t + \Delta t$ and, secondly, correction with second order precision at time $t + \Delta t$.

In the prediction step, where progressive differences in x and y are applied, the solution vector was obtained by:

$$\bar{U}_{i,j}^{t+\Delta t} = U_{i,j}^{t} - \frac{\Delta t}{\Delta x}\left(E_{i+1,j}^{t} - E_{i,j}^{t}\right) - \frac{\Delta t}{\Delta y}\left(F_{i,j+1}^{t} - F_{i,j}^{t}\right) \tag{20}$$

The solution vector for the correction step was calculated with backward differences in x and y:

$$U_{i,j}^{t+\Delta t} = \frac{1}{2}\left[U_{i,j}^{t} + \bar{U}_{i,j}^{t+\Delta t} - \frac{\Delta t}{\Delta x}\left(\bar{E}_{i,j}^{t+\Delta t} - \bar{E}_{i-1,j}^{t+\Delta t}\right) - \frac{\Delta t}{\Delta y}\left(\bar{F}_{i,j}^{t+\Delta t} - \bar{F}_{i,j-1}^{t+\Delta t}\right)\right] \tag{21}$$

MacCormack's method has an explicit formulation, so it is necessary to use a stability criterion for the time step. In this work, a version of the Courant–Friedrichs–Lewy (CFL) described by Anderson (1995) was used, where the time step (Δt) was calculated by

$$\Delta t = min[CFL(\Delta t_{CFL})]_{i,j} \tag{22}$$

$$(\Delta t_{CFL})_{i,j} = \left[\frac{|u_{i,j}|}{\Delta x} + \frac{|v_{i,j}|}{\Delta y} + a_{i,j}\sqrt{\frac{1}{\Delta x^2} + \frac{1}{\Delta y^2}} + 2\nu'_{i,j}\left(\frac{1}{\Delta x^2} + \frac{1}{\Delta y^2}\right)\right]^{-1} \tag{23}$$

and

$$\nu'_{i,j} = \frac{\max\left(\mu_{i,j}, \lambda + 2\mu_{i,j}, \frac{\gamma\mu_{i,j}}{Pr}\right)}{\rho_{i,j}} \tag{24}$$

As one can notice, the Courant number constrains the time resolution and its value should be decreased in order to the iterations stay closer to facilitate convergence with the disvantage of increasing the number of iterations. The Courant number's recommendations vary as the types of simulations vary, but the most recommended practice is using values less than 1. In fact, this work used $0{,}3 \leq CFL \leq 0{,}8$.

2.3 NUMERICAL MODELING

In Figure 3, boundary conditions for the computational domain are described considering the incidence of a shock wave on the flat plate.

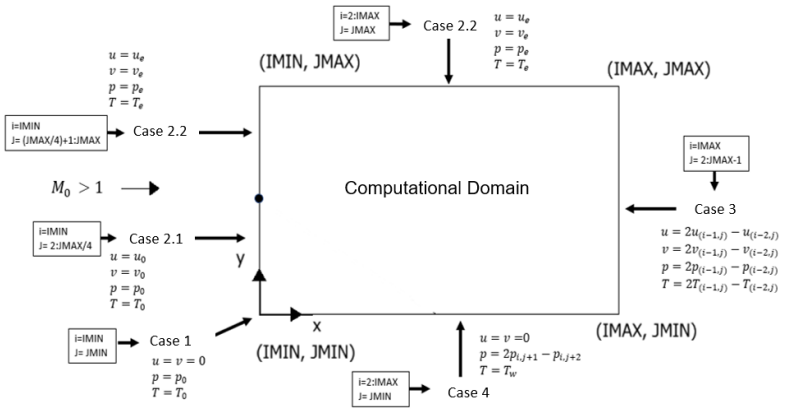

Figure 3 Boundary conditions of the computational domain considering the impact of a shock wave, adapted (ANDERSON JR, 1995).

The case 1 represents the leading edge and freestream pressure and temperature were used. The no-slip condition was assumed, $u = v = 0$.

The case 2 represents the top and left boundaries (except the leading edge). In case 2.1, it was used the freestream properties. In case 2.2, it was used the properties after the oblique shock wave. These properties were calculated by the oblique plane shock wave theory (ANDERSON JR, 1990). The shock wave angle (β) was calculated with:

$$\tan\theta = 2\ \cot\beta \left[\frac{M_0^2 \operatorname{sen}^2\beta - 1}{M_0^2(\gamma + \cos 2\beta) + 2}\right] \tag{25}$$

where θ and M_0 are the ramp angle and the freestream Mach number, respectivelly.

The Mach number, density, pressure and temperature downstream the oblique shock wave were calculated by the equations below:

$$M_e = \frac{\sqrt{\dfrac{(M_0\ \ sen\,\beta)^2 + \dfrac{2}{(\gamma-1)}}{\dfrac{2\,\gamma}{(\gamma-1)}(M_0\ \ sen\,\beta)^2 - 1}}}{sen(\beta-\theta)} \tag{26}$$

$$\rho_e = \rho_0 \frac{(\gamma+1)M_0^2\, sen^2\,\beta}{2 + (\gamma-1)M_0^2\, sen^2\,\beta} \tag{27}$$

$$p_e = p_0\left[1 + \frac{2\gamma}{\gamma+1}(M_0^2\, sen^2\,\beta - 1)\right] \tag{28}$$

$$T_e = \frac{p_e}{R\rho_e} \tag{29}$$

where is the γ is the ratio of specific heats.

The case 3 represents the interior points of the exit plane and the properties were calculated using extrapolation by:

$$p_{i,j} = 2p_{i-1,j} - p_{i-2,j} \tag{30}$$

$$u_{i,j} = 2u_{i-1,j} - u_{i-2,j} \tag{31}$$

$$v_{i,j} = 2v_{i-1,j} - v_{i-2,j} \tag{32}$$

and

$$T_{i,j} = 2T_{i-1,j} - T_{i-2,j} \tag{33}$$

The case 4 represents the contour of the plate surface (exception of the leading edge). The non-slip condition was considered ($u = v = 0$), wall temperature (T_w) and pressure was calculted using extrapolation as

$$p_{i,j} = 2p_{i,j+1} - p_{i,j+2} \tag{34}$$

3. RESULTS

The simulation of supersonic flow was performed considering the incidence of an oblique shock wave on a flat plate, with the test matrix depicted in Table 1. Mach number varied from 3 to 6 and flow deflection angles from 10 to 20 deg to freestream properties (Table 2) at constant temperature ($T_w = T_0$) and adiabatic wall.

Table 1 Test matrix considering the incidence of an oblique shock wave.

Mach Number	**Flow Deflection Angles**		
	10°	**15°**	**20°**
3	x	x	x
4	x	x	x
5	x	x	x
6	x	x	x

Table 2 Freestream flow properties.

$T_0\ [K]$	$p_0\ [kPa]$	γ	$R\ [J/(kg \cdot K)]$
288.16	101.325	1.4	287

The Figures 4, 5, 6, 7, 8 and 9 show temperature , pressure, Mach number, skin friction coefficient and heat flux, respectively. The x-axis coordinate was adimensionlized with respect to the total flat plate length ($LHORI$) and the y-axis coordinate with respect to the vertical height of the domain ($LVERT$). It is observed that the increase in the Mach number at freestream and the angle of the incident shock wave cause higher values of pressure, temperature and heat flux at the trailing edge. Pressure and temperature have higher values closer to the plate (at lower values of $y/LVERT$). This happens due the viscous dissipation on the surface of the plate, which causes an increase in temperature, pressure and heat flux in the flow field inside the boundary layer. The properties have severe variations close to the plate and then reach stable values far from the wall.

The separation of the boundary layer can be evidenced through the negative values of the skin friction coefficient at Mach 3, 15° ($0.275 \leq x/LHORI \leq 0.319$) and 20° ($0.087 \leq x/LHORI \leq 0.29$), at Mach 4, 20° ($0.188 \leq x/LHORI \leq 0.29$) and at Mach 5, 20° ($0.246 \leq x/LHORI \leq 0.261$). It can be seen that the increase in Mach number and the decrease in the angle of flow deflection cause the reduction of the length of separation zone.

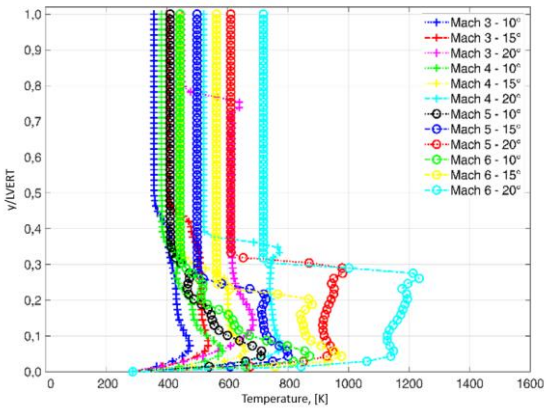

Figure 4 Temperature at $x/LHORI = 1$ along $y/LVERT$.

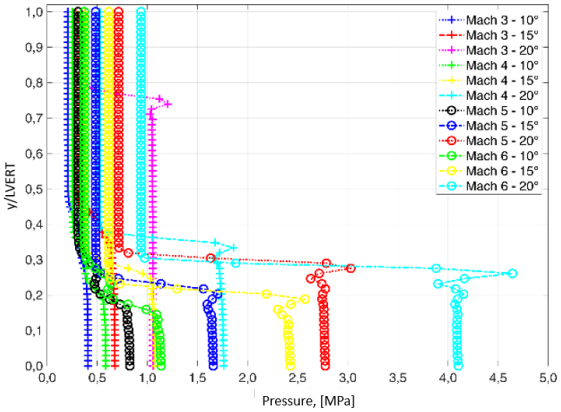

Figure 5 Pressure at $x/LHORI = 1$ along $y/LVERT$.

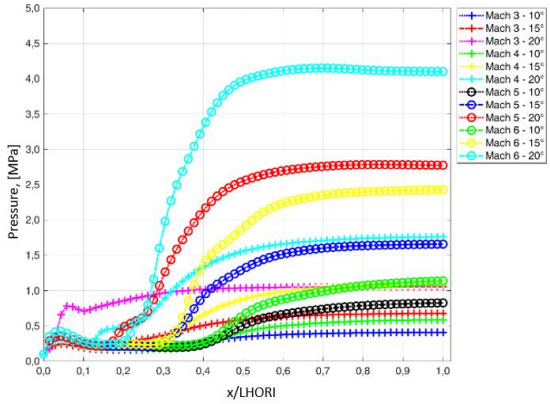

Figure 6 Wall pressure along $x/LHORI$.

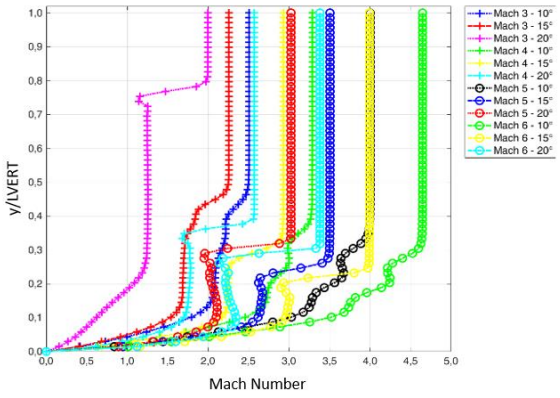

Figure 7 Mach number at $x/LHORI = 1$ along $y/LVERT$.

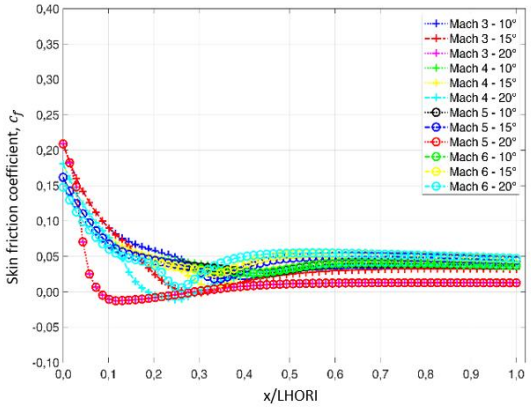

Figure 8 Wall skin friction coefficient along $x/LHORI$.

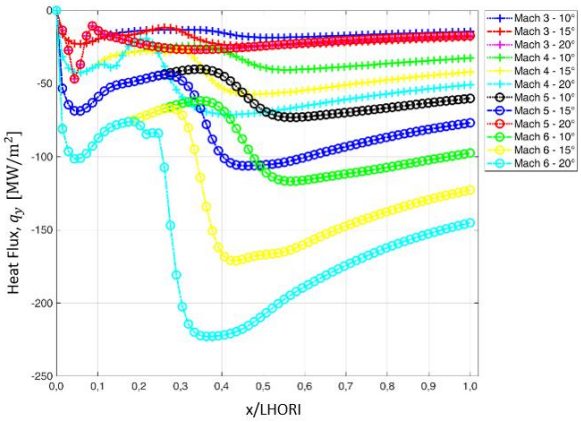

Figure 9 Wall heat flux along $x/LHORI$.

The Figures 10, 11 and 12 show skin friction coefficient, pressure and x-velocity behavior at Mach 4, respectively. There is no separation of the boundary layer at 10° and 15°. Regarding Figure 11, at 20°, there is increased pressure, followed by a plateau and then a rise again. This plateau is typical of regions of separation and the final growth represents the reattaching of the boundary layer. This same phenomenon is observed in the cases at Mach 3, 15° and 20° and Mach 4, 20°. In Figure 12, analyzing the angle of deflection of 20°, it can be seen that the x-velocity near wall decreases at the beginning of the leading edge. At $x/LHORI =$ 0,188, the x-velocity is zero and keeps decreasing for negative numbers ($\left(\frac{du}{dy}\right|_w < 0$) until $x/LHORI =$ 0.261. At this location, the velocity near the wall has negative values, indicating change in direction.

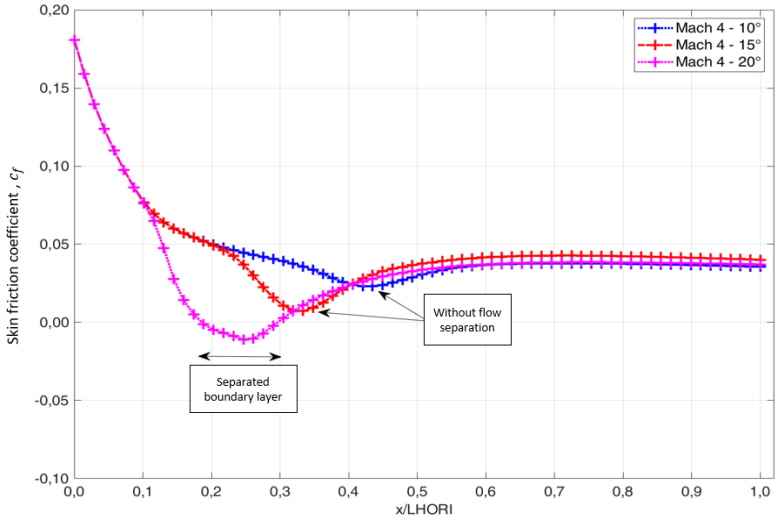

Figure 10 Wall skin friction coefficient along $x/LHORI$ at Mach number 4.

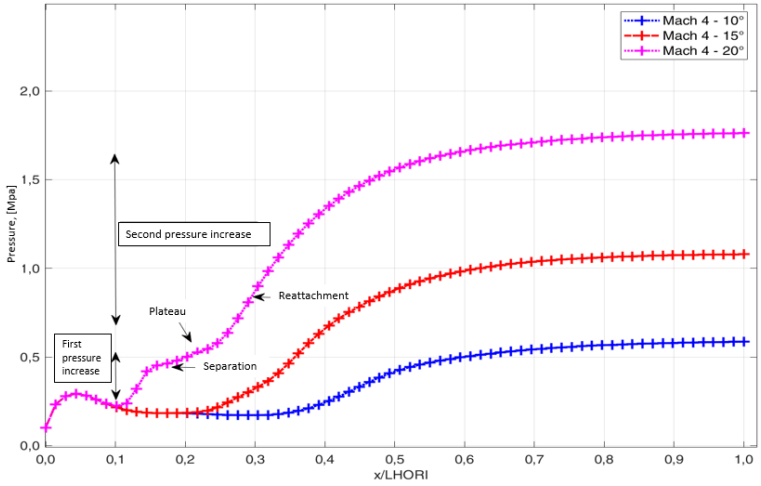

Figure 11 Wall pressure along $x/LHORI$ at Mach number 4.

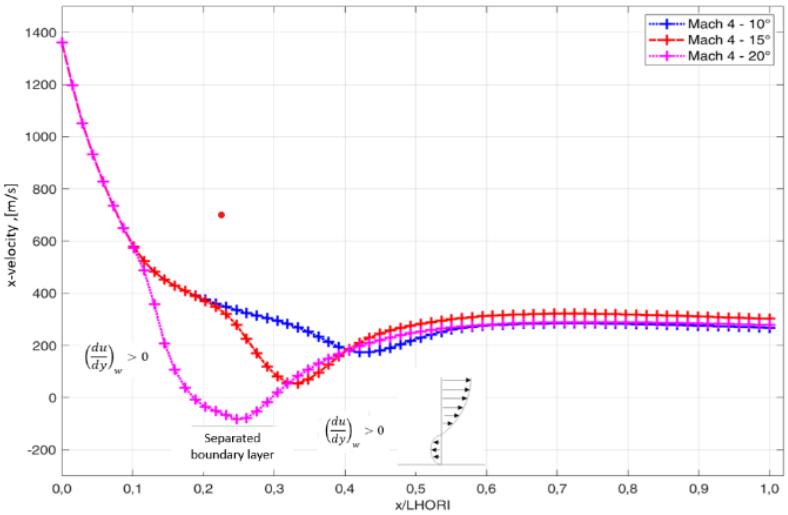

Figure 12 Near wall velocity along $x/LHORI$ at Mach number 4.

The Figures 13, 14, 15, 16, 17, 18, 19 and 20 show the pressure, temperature, Mach number and numerical Schlieren for Mach number 4. For the sake of completeness, comparisons between the properties distribuitions for the cases of flow deflections of 10° (no separation) and 20° (with separation) were performed. Pressure gradients were not high

enough to cause the boundary layer separation at 10°. In Figure 17, it was possible to notice the presence of a supersonic region and a subsonic region close to the wall of the plate, due its no-slip condition. With an angle of deflection 20°, there is an abrupt reduction in speed due to changes in momentum and energy, see Figure 19. Analyzing property distributions, it can be seen that the shock wave impinges on the wall and is reflected as expansion waves. This phenomenon causes pressure increase and causes the inversion and separation of the boundary layer. The boundary layer has an elevation, the flow expands and then the boundary layer reattaches. Moreover, there is the formation of compression waves, which collide and form the reflected shock near the separation point, see Figure 19.

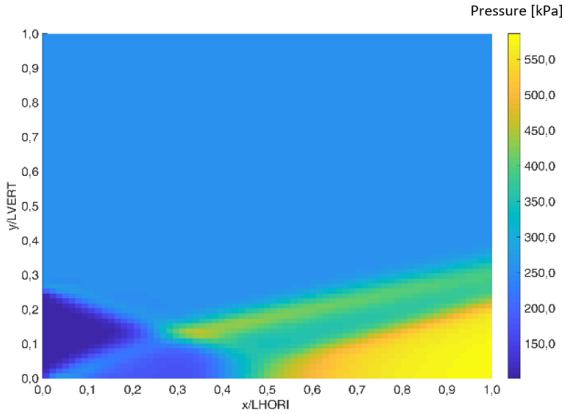

Figure 13 Pressure distributions at Mach number 4 and 10°.

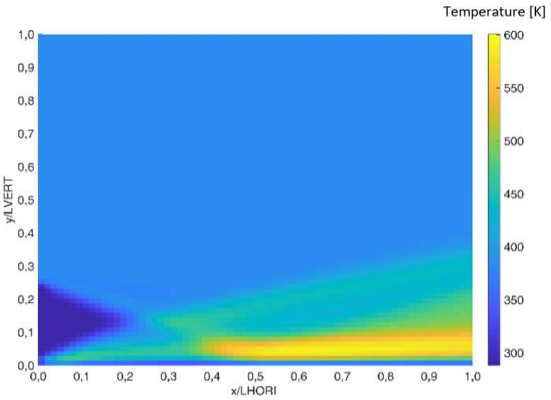

Figure 14 Temperature distributions at Mach number 4 and 10°.

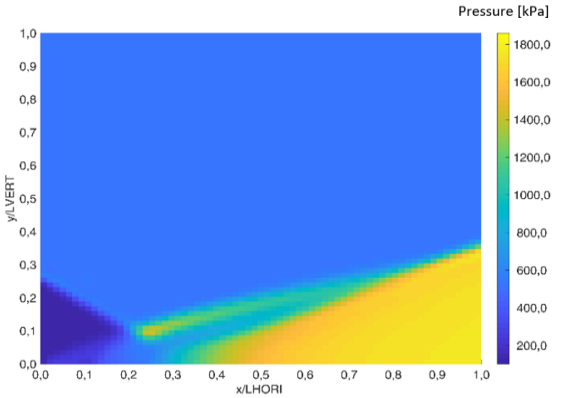

Figure 15 Pressure distributions at Mach number 4 and 20°.

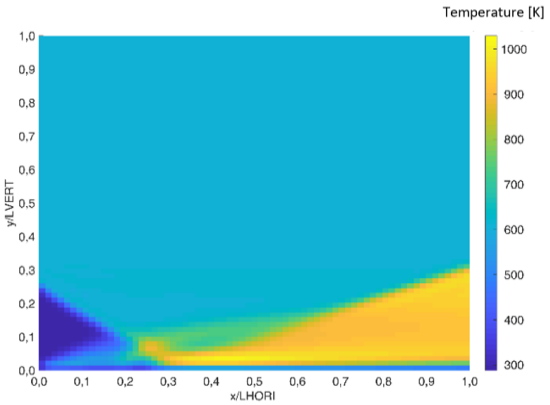

Figure 16 Temperature distributions at Mach number 4 and 20°.

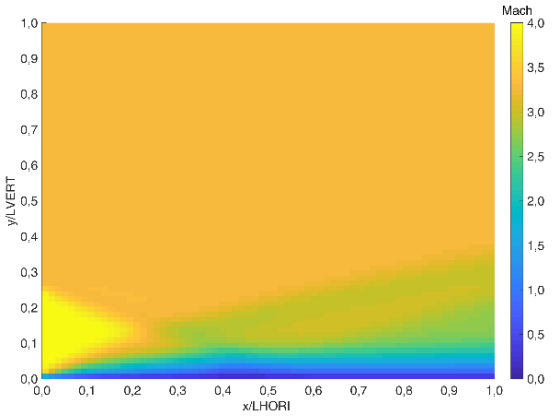

Figure 17 Mach number distributions at Mach number 4 and 10°.

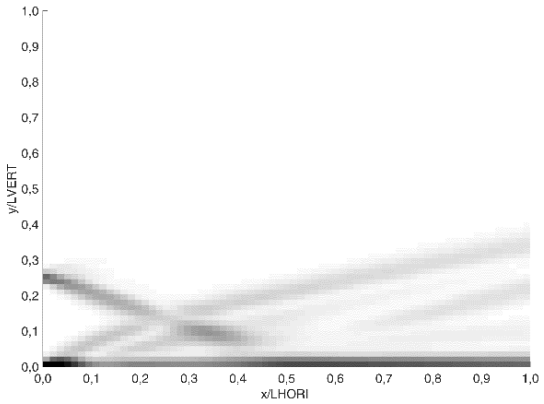

Figure 18 Numerical Schlieren at Mach number 4 and 10°.

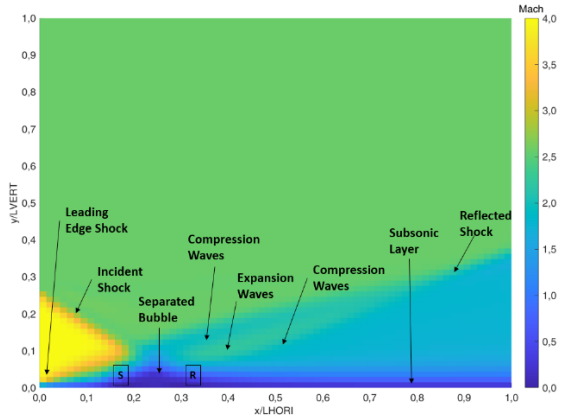

Figure 19 Mach number distributions at Mach number 4 and 20°.

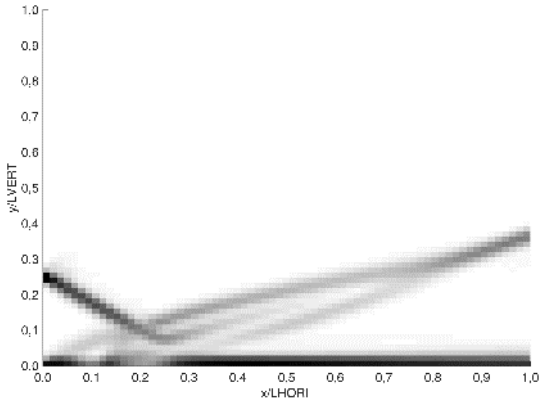

Figure 20 Numerical Schlieren at Mach number 4 and 20°.

4. CONCLUSION

The objective of this work was to study the limits of the geometry angles to predict the conditions which the boundary layer separation occurs when it interacts with an impinging shock wave. A code was developed using the MacCormack method to simulate the supersonic flow. The following remarks can be made:

- The increase in the Mach number of freestream and the angle of the incident shock wave cause higher values of pressure, temperature and heat flux at the trailing edge. Pressure and temperature have higher values near the plate, and they have severe variations near the plate.
- The boundary layer separation was observed at Mach 3, 15° and 20°, at Mach 4, 20°, and at Mach 5, 20°. The separation can be evidenced through the negative values of the skin friction coefficient, negative velocity in the wall and the plateau of the pressure curve. In these conditions, it was noticed that the shock wave impinges on the wall and is reflected, increasing the pressure, causing the inversion of the flow and separation of the boundary layer.
- The increase in Mach number and the decrease in the angle of deflection lead to a reduction in the separation zone.

As future work, the impinging shock wave/boundary layer interaction will be analyzed using a shock tunnel to visualize the phenomenon and compare it with the numerical results.

5. ACKNOWLEDGEMENTS

The first author would like to express gratitude for financial support to the project COMAER PROPHIPER 14-X and the Coordenação de Aperfeiçoamento de Pessoal de Nível Superior - Brasil (CAPES) - Finance Code 001.

6. REFERENCES

ANDERSON JR, D. **Computational Fluid Dynamics:** The Basics with Applications. 1. ed. New York, NY: MacGraw- Hill, 1995.

ANDERSON JR, J. D. **Modern Compressible Flow:** With Historical Perspective. 2. ed. New York: McGraw-Hill, 1990.

BABINSKY, H.; HARVEY, J. K. **Shock Wave – Boundary- Layer Interactions**. 1. ed. New York: Cambridge University Press, 2011.

GAITONDE, D. V. Progress in ShockWave / Boundary Layer Interactions. In: 43rd Fluid Dynamics Conference, 2013, **Proceedings...** San Diego, CA: American Institute of Aeronautics and Astronautics, 24-27 June 2013.

STOKES, G. G. On the Theories of the Internal Friction of Fluids in Motion and of the Equilibrium and Motion of Elastic Solids. In: STOKES, G. G. **Mathematical and Physical Papers**. New York: Cambridge University Press, v. 1, 1880. p. 75-129.

7. RESPONSIBILITY NOTICE

The authors are the only responsible for the printed material included in this paper.